JACS
JOURNAL OF THE AMERICAN CHEMICAL SOCIETY

pubs.acs.org/JACS Article

High-Throughput Electrochemical Delamination of Two-Dimensional Covalent Organic Frameworks

Tong Ju, Xiansong Shi,* Zhenshu Si, Tianci Feng, Jianghai Long, Congcong Yin, Zhe Zhang, and Yong Wang*

Cite This: *J. Am. Chem. Soc.* 2025, 147, 23809−23818

ABSTRACT: Porous crystalline nanosheets of two-dimensional covalent organic frameworks (2D COFs) possess intriguing structural features and extensive application potential. However, the scalable and efficient synthesis of well-crystallized COF nanosheets remains challenging despite recent advances in exfoliation and in situ growth techniques. Here we report a high-throughput electrochemical strategy that nondestructively delaminates polycrystalline 2D COF films into large nanosheets with long-range crystallographic order. This method achieves a remarkable delamination productivity of 100 mg h^{-1}, yielding crystalline nanosheets that are readily dispersible across various solvents including water. Principal component analysis reveals solvent permittivity and polarity, along with film wettability, as critical factors governing the delamination efficiency. Complementary diffraction, spectroscopy, and electron microscopy studies elucidate a synergistic delamination mechanism involving molecular preintercalation, framework protonation, and electrolysis-driven gas evolution. Leveraging the intrinsic microporosity and excellent solution processability of these nanosheets, we demonstrate their utility in producing membranes for efficient antibiotic desalination. This work advances the scalable synthesis of crystalline COF nanosheets, broadening the application toolkit of COFs.

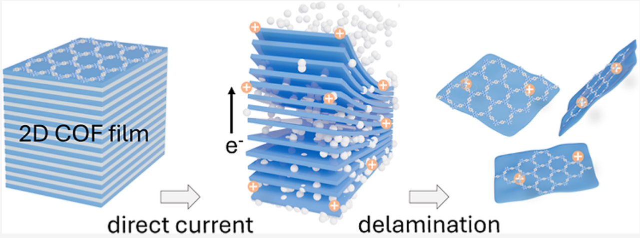

■ INTRODUCTION

Since the advent of single-layer graphene,[1] two-dimensional (2D) materials have revolutionized multiple fields, including catalysis, energy storage, and separation technologies, owing to their exceptional electronic, mechanical, and surface properties.[2−4] Over the past decade, significant progress has been made in the synthesis of diverse 2D nanomaterials, such as transition metal dichalcogenides (TMDs),[5,6] hexagonal boron nitride (h-BN),[7,8] MXenes,[9,10] and covalent organic frameworks (COFs).[11,12] 2D COFs have garnered increasing interest as a class of layered, crystalline organic materials, characterized by atomically precise structures and tunable functionalities.[13−15] Their high porosity, chemical stability, and customizable frameworks render them highly promising for applications in energy and environmental fields,[16−19] offering advantages that are often unattainable with conventional nonporous 2D analogues.[20]

Despite these promising attributes, conventional COF synthesis methods predominantly yield polycrystalline powders that are insoluble and intractable, significantly limiting their processability and application.[21−23] To address this limitation, efforts have been directed toward developing COF nanosheets in solution, facilitating their scalable processing and facile incorporation into device architectures. Existing methods for producing COF nanosheets can be categorized into bottom-up and top-down approaches. Bottom-up strategies, such as solvothermal synthesis using templates or colloidal precursors, allow the direct growth of nanosheets from molecular building blocks but often suffer from insufficient crystallinity and structural imperfections.[24−26] In contrast, top-down methods, including mechanical[27,28] and liquid-phase exfoliation,[29−31] produce nanosheets by delaminating bulk layered COFs. While these approaches have demonstrated success in generating COF nanosheets, they typically involve labor-intensive procedures, suffer from limited scalability, and result in nanosheets with compromised crystallinity. Thus, developing a facile, efficient, and scalable method for producing high-quality COF nanosheets remains a significant challenge.

Electrochemical delamination has emerged as a highly promising alternative for producing solution-processable 2D materials, offering a controllable, efficient, and scalable strategy.[32−34] Unlike conventional destructive exfoliation techniques, electrochemical exfoliation facilitates nondestructive delamination with minimal structural compromise, resulting in high-quality nanosheets with well-defined lateral

Received: April 9, 2025
Revised: June 3, 2025
Accepted: June 17, 2025
Published: June 25, 2025

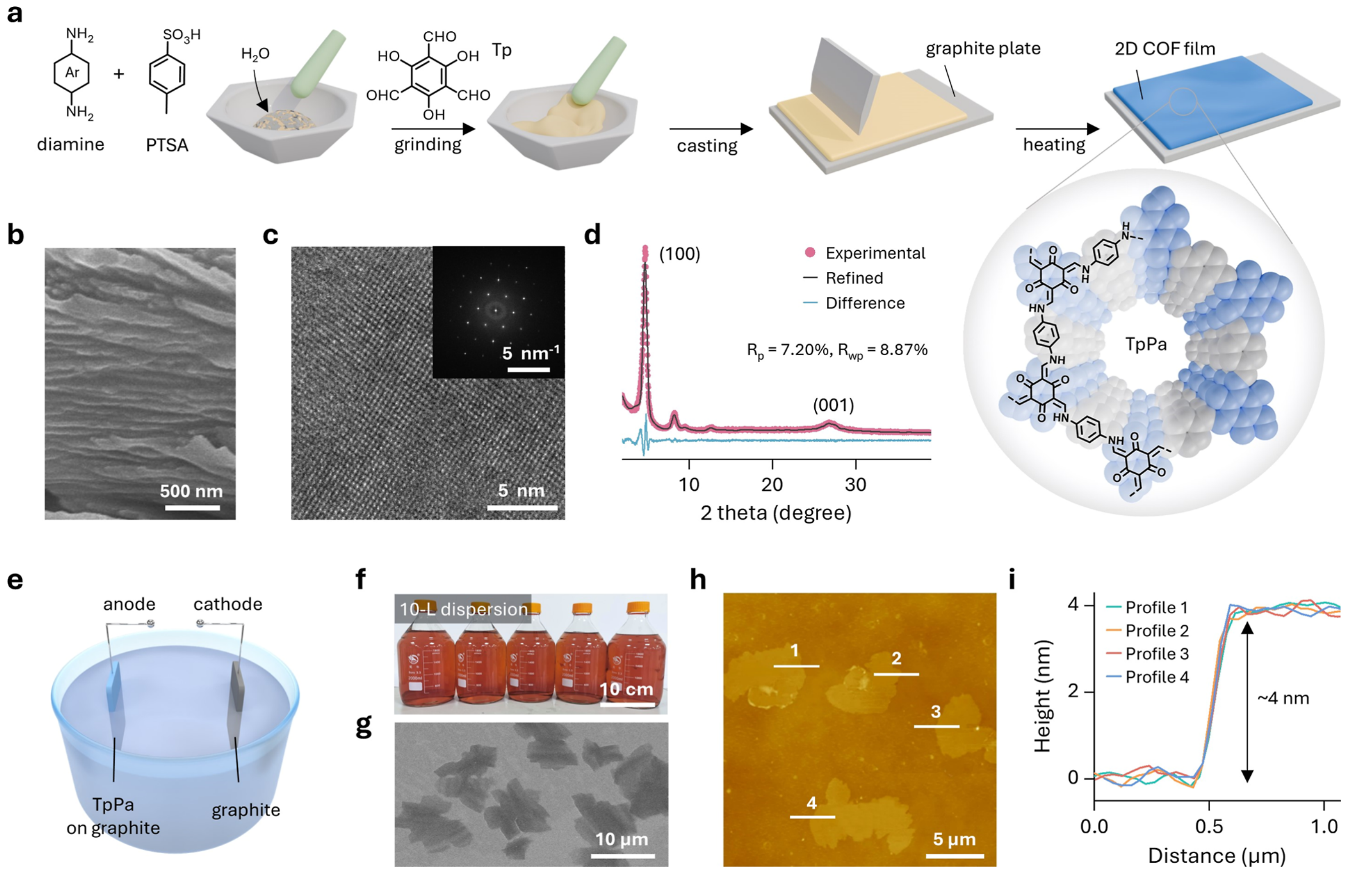

Figure 1. Crystalline 2D COF films and nanosheets. (a) Schematic illustration of the polycrystalline 2D COF film preparation. (b) Cross-sectional SEM image of the TpPa film. (c) TEM and SAED images of the TpPa film. (d) Experimental and refined PXRD patterns of the TpPa film. (e) Schematic diagram of the electrochemical delamination. (f) Photograph of TpPa-200 dispersions. (g) SEM image of TpPa-200. (h) AFM image and (i) the corresponding height profiles of TpPa-200.

dimensions and tunable thickness.[35−37] Compared to mechanical or liquid-phase exfoliation, electrochemical delamination provides additional advantages, including adjustable exfoliation rates, single-step processing, and facile operation under ambient conditions, making it highly suitable for large-scale production.[38] While electrochemical exfoliation has been extensively employed for inorganic layered materials, its implementation on COFs remains largely unexplored due to the scarcity of established methodologies specifically designed for COFs.[39]

In this study, we report the efficient and scalable synthesis of crystalline COF nanosheets via high-throughput electrochemical delamination of polycrystalline 2D COF films. We achieved high-quality COF nanosheet dispersions in both organic and aqueous media by optimizing the electrolyte composition and direct current bias. Principal component analysis, combined with comprehensive structural determinations, reveals unambiguous correlations among delamination conditions, efficiency, and crystallographic order of the resulting nanosheets. Moreover, mechanistic studies uncover a synergistic delamination process driven by the applied direct current bias, providing valuable insights into the exfoliation of two-dimensionally stacked COFs. We further show the practical effectiveness of these porous crystalline nanosheets in fabricating separation membranes that exhibit efficient antibiotic desalination.

RESULTS AND DISCUSSION

Polycrystalline 2D COF Films. We fabricated polycrystalline 2D COF films on graphite plates by using a stepwise heating approach (Figure 1a). The films were formed through Schiff-base condensation, wherein a selection of diamines covalently bonded with 1,3,5-triformylphloroglucinol (Tp) under the catalysis of *p*-toluenesulfonic acid (PTSA) to form imine-linked frameworks. PTSA was strategically chosen to facilitate layer-by-layer growth of 2D COF films, which is decisive for effective electrochemical delamination. Scanning electron microscopy (SEM) images reveal that PTSA promotes the formation of the layered TpPa film by inducing fibrillar intermediates upon mixing with phenylenediamine (Pa) (Figure S1). These fibers act as structural templates that spatially confine the subsequent Schiff-base condensation with Tp,[40] thus directing the growth of well-stacked films (Figures 1b, S2, and S3). Fourier-transform infrared (FTIR) spectra identify the formation of a keto-amine structure of the TpPa film,[41] with characteristic stretching vibrations at 1586 cm^{-1} (C=C) and 1260 cm^{-1} (C−N) (Figure S4). X-ray photoelectron spectroscopy (XPS) analysis confirmed the effective removal of PTSA from the TpPa film after solvent washing (Figure S5). Transmission electron microscopy (TEM) images provide evidence of a laminated structure and high crystallinity of the film, with clear lattice fringes (Figures 1c, S6). The selected area electron diffraction (SAED) pattern displays well-defined diffraction spots that align with the theoretical lattice

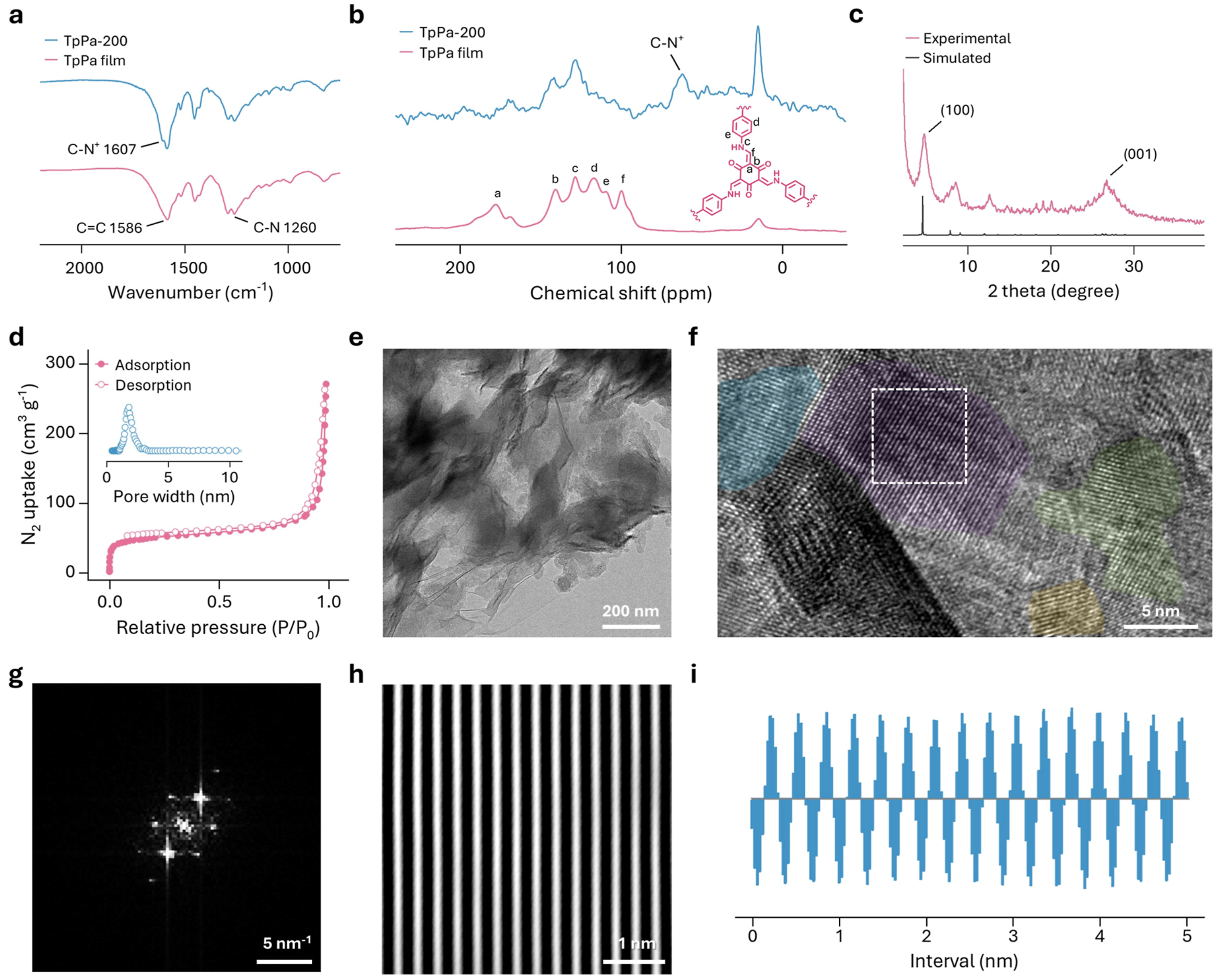

Figure 2. Structural analysis of TpPa-200. (a) FTIR and (b) ^{13}C solid-state NMR spectra of the TpPa film and TpPa-200. (c) Experimental and simulated PXRD patterns. (d) 77 K N_2 sorption isotherms. (e) TEM image. (f) False-color high-resolution TEM image. (g) FFT pattern of the boxed region in (f). (h) Inverse FFT image and (i) interlayer spacing analysis. Inset in (d) shows the pore width distribution of TpPa-200.

model, confirming the crystalline nature of our film (inset in Figure 1c).

We performed powder X-ray diffraction (PXRD) measurements to assess the film crystallinity. The PXRD pattern shows intense diffraction peaks from the (100) and (001) crystal planes at 2-theta values of 4.72° and 26.80°, respectively (Figure 1d). Pawley refinement reveals strong agreement between the experimental and refined PXRD patterns, with R_p = 7.20% and R_{wp} = 8.87%. To determine the film porosity, we performed N_2 sorption measurements at 77 K. The significant N_2 uptake at low relative pressures indicates pronounced microporosity of the film (Figure S7). Its Brunauer−Emmett−Teller (BET) surface area reaches a notable value of 1740 m^2 g^{-1}, surpassing previously reported COF membranes/films with comparable pore sizes (1.36−1.93 nm) (Table S1). The versatility of this fabrication strategy was demonstrated by extending it to other crystalline 2D COF films including TpPa-SO_3H, TpBD, and TpAzo (Figure S8). FTIR and PXRD analyses confirm the formation of polycrystalline keto-amine COF films with distinct diffraction peaks corresponding to the (100) and (001) planes (Figures S9 and S10). Moreover, N_2 sorption studies at 77 K corroborate the microporous nature of these 2D COF films (Figure S11).

Electrochemical Delamination of Polycrystalline 2D COF Films. To implement electrochemical delamination, the as-synthesized polycrystalline COF films were integrated into a setup where the film acted as the anode, a neat graphite plate as the cathode, and a 0.01 M PTSA ethanol solution as the electrolyte (Figure 1e). The resultant COF nanosheets were designated as COF-X, where X denotes the applied current (mA). Applying a direct current bias of 200 mA for 60 min yielded an orange-red TpPa-200 nanosheet dispersion with a high concentration of approximately 200 mg L^{-1}. This thick dispersion can be readily diluted with water to produce a 10 L solution showing a distinct Tyndall effect (Figures 1f and S12). Notably, the diluted solution remains stable for at least 4 months without visible aggregation or precipitation (Figures S12 and S13), suggesting its exceptional stability for practical applications. Zeta potential analysis reveals that the nanosheets carry a positive surface charge (Figure S14), which promotes stable dispersion through electrostatic repulsion. This positively charged surface also leads to slight adsorption of PTSA on TpPa-200 (Figure S15). Morphological character-

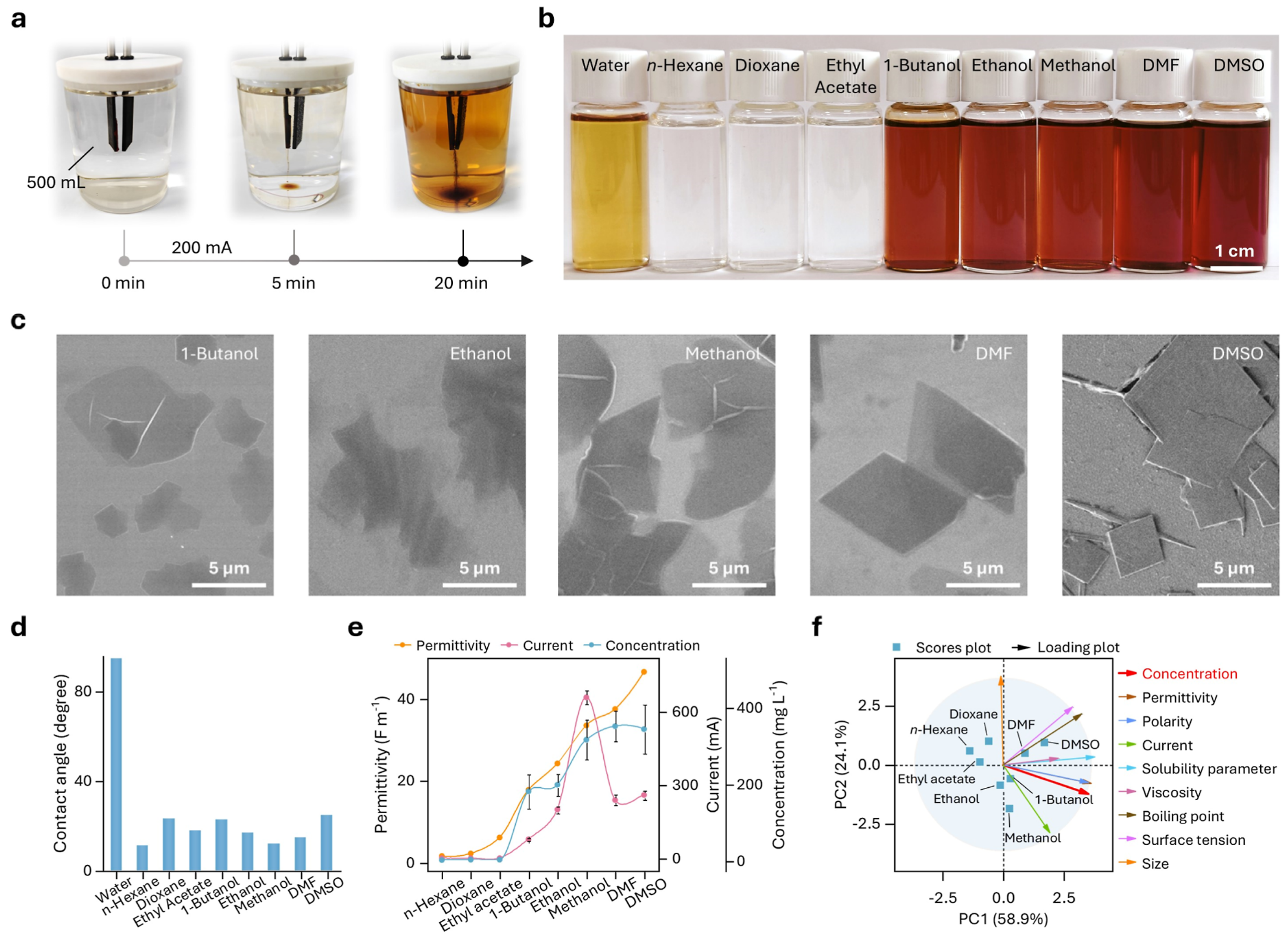

Figure 3. Solvent-dependent electrochemical delamination. (a) Photographs of the electrochemical delamination in ethanol. (b) Photograph of the TpPa dispersions obtained in different solvents. (c) SEM images of the TpPa nanosheets obtained in different solvents. (d) Contact angles of the TpPa film toward different solvents. (e) Correlation among solvent permittivity, generated current, and nanosheet concentration. (f) PCA of solvent properties and their impact on the delamination efficiency.

istics of TpPa-200 were examined by using SEM and atomic force microscopy (AFM). SEM images depict a smooth, sheet-like morphology with large lateral dimensions spanning ∼5−∼14 μm (Figures 1g, S16). AFM measurements reveal an ultrathin, uniform structure with an average thickness of ∼4 nm (Figure 1h,i). This electrochemical delamination approach can be extended to TpPa-SO_3H, TpBD, and TpAzo films, all of which yield well-dispersed solutions (Figure S17). SEM imaging confirms the nanosheet morphology across these cases (Figure S18), while AFM analyses determine consistently low thicknesses below 5 nm (Figure S19). These results highlight the efficacy and scalability of this electrochemical protocol for producing high-quality, thickness-uniform nanosheets with broad applicability across diverse 2D COFs.

Structural Characteristics of TpPa Nanosheets. Comprehensive investigations were conducted to elucidate the structural characteristics of the electrochemically delaminated TpPa film. FTIR spectra show the preservation of the keto-enamine structure in TpPa-200 (Figure 2a). Notably, a new stretching vibration appears at 1607 cm^{-1}, which can be attributed to $C-N^+$ formed through framework protonation during electrochemical delamination (Figure S20).[39] Further validation is provided by ^{13}C solid-state nuclear magnetic resonance (NMR) spectra, which show an additional characteristic peak of $C-N^+$ at the chemical shift of 61.7 ppm (Figure 2b).[42] This protonation is facilitated by the lone pair of electrons on the nitrogen atom within the enamine moieties of the TpPa framework. In the electrochemical environment, proton generation occurs through the dissociation of PTSA and ethanol, driven by polarization effects and stabilization of charged species.[39] These protons interact with the nitrogen lone pairs, inducing framework protonation, as corroborated by the aforementioned zeta potential result.

Next, we employed PXRD to assess the crystallinity of TpPa-200. The diffraction pattern shows distinct peaks from the (100) and (001) crystal planes at 4.8° and 26.7°, respectively (Figure 2c), indicating preserved long-range order. N_2 sorption measurements at 77 K determine a significant BET surface area of approximately 182 $m^2\ g^{-1}$ for TpPa-200 (Figure 2d). The rapid gas uptake at low relative pressures highlights its highly microporous structure with a calculated pore diameter of ∼1.83 nm. The crystallinity and microporosity of TpPa-200 remain largely preserved after 6 months of storage, indicative of its high chemical stability (Figure S21). TEM imaging shows the corrugated morphology of TpPa-200 (Figures 2e and S22), consistent with the flexible nature of ultrathin nanosheets. High-resolution TEM images further validate their crystalline structure, showing well-defined

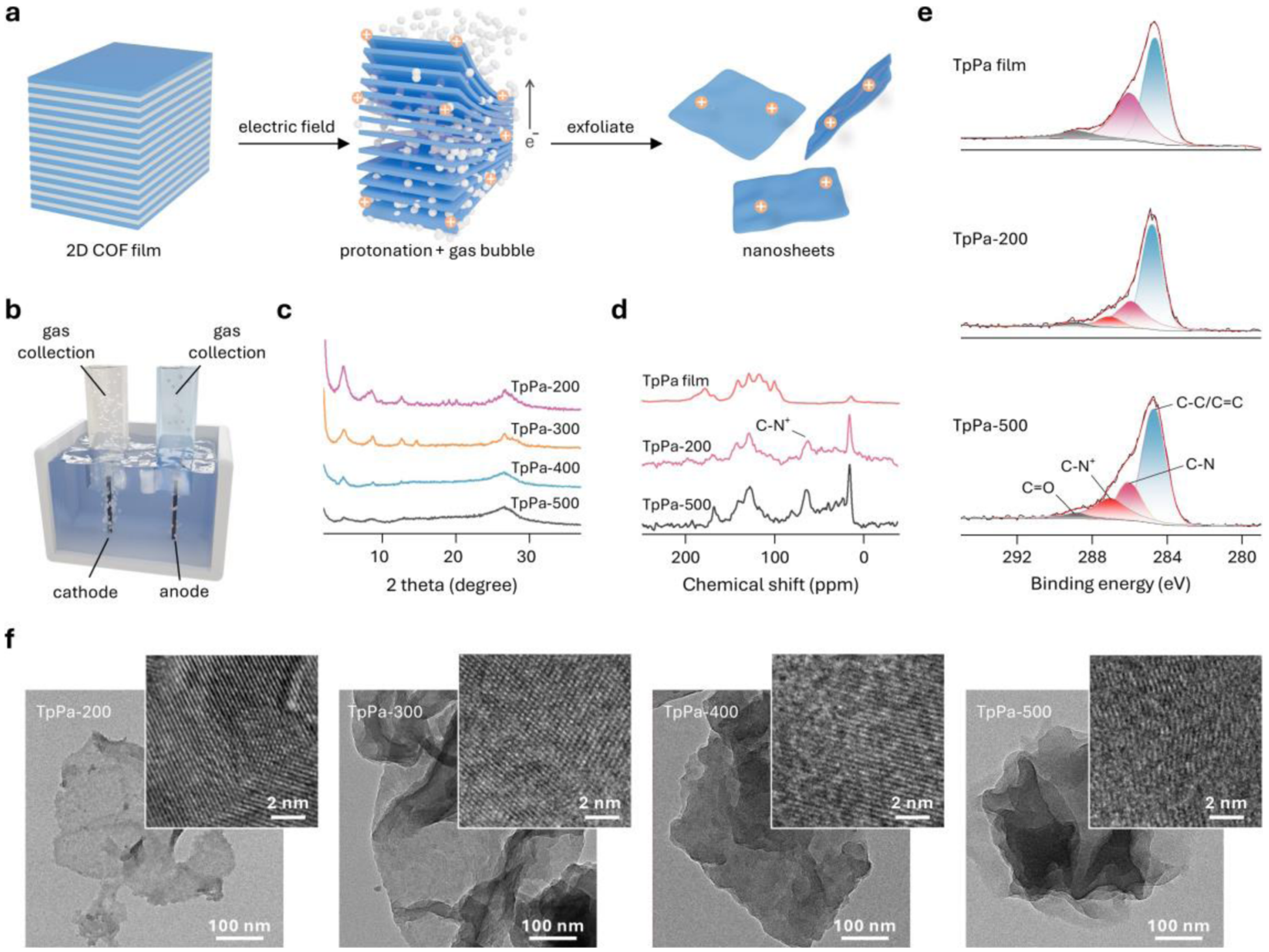

Figure 4. Current-dependent electrochemical delamination. (a) Schematic illustration of the delamination process. (b) Gas collection at the cathode and anode. (c) PXRD patterns, (d) ^{13}C solid-state NMR spectra, (e) XPS C 1s spectra, and (f) TEM images of the TpPa nanosheets produced under different currents.

lattice fringes across different regions (Figures 2f and S23). False-color fringes show directional variations, indicative of a polycrystalline structure. Fast Fourier transform (FFT) patterns exhibit sharp and discrete diffraction spots, signifying a well-ordered framework (Figures 2g and S24). The inverse FFT image shows consistent lattice fringes with a spacing of 0.33 nm, corresponding to the distance of the (001) crystal plane (Figure 2h,i). These findings demonstrate that TpPa-200 largely maintains its intrinsic crystallinity and microporosity, matching the nondestructive electrochemical strategy. This approach outperforms conventional delamination methods, which often yield COF nanosheets with compromised structural order,[23,27,43] offering a scalable and reliable route to crystalline COF nanosheets.

Effect of Solvents on Electrochemical Delamination. The efficiency of electrochemical delamination is influenced by multiple factors, with the choice of solvent playing a critical role. Using ethanol as a model solvent, we demonstrated its effectiveness in promoting delamination. As shown in Figure 3a, the delamination process was conducted in 500 mL of ethanol containing 0.01 M PTSA. Initially, the ethanol solution appeared colorless and transparent. Upon applying a 200 mA current for 5 min, the crystalline TpPa film begins to disintegrate and disperse into ethanol. After 20 min, the solution turns orange−red, suggesting significant delamination. After 1 h, a uniform, high-concentration dispersion of TpPa-200 nanosheets is achieved with a high productivity of 100 mg h^{-1} (Figure S25), surpassing conventional COF exfoliation methods (Figure S26). To quantify the delamination process, ultraviolet−visible (UV−vis) spectroscopy was performed on the samples collected at 1 min intervals from a 50 mL electrolytic cell. The spectra determine a near-linear increase in nanosheet concentration during the first 10 min (Figure S27), with a prominent delamination rate of ~14.1 mg L^{-1} min^{-1}.

Solvent permittivity was identified as a key factor influencing the delamination efficiency. To evaluate its impact, electrochemical delamination was performed in solvents of varying permittivity under identical conditions (30 V, 1 h, 0.01 M PTSA) (Table S2). The resulting solutions exhibit distinct color variations (Figure 3b). High-permittivity solvents (water, *N*,*N*-dimethylformamide (DMF), and dimethyl sulfoxide (DMSO)) and moderate-permittivity solvents (1-butanol, ethanol, and methanol) facilitate the delamination, yielding nanosheet dispersions (Figures 3c and S28). In contrast, the use of low-permittivity solvents, such as *n*-hexane, dioxane, and ethyl acetate, yields colorless solutions, indicating negligible delamination. Despite its higher permittivity over methanol, water delivers relatively low delamination efficiency, likely due to the poor wettability of the TpPa film by water. The hydrophobic aromatic framework of TpPa imparts a relatively hydrophobic surface, leading to weak interactions with water (Figure S29). By contrast, organic solvents all exhibit high affinity for the TpPa film, as evidenced by significantly lower contact angles (Figures 3d and S30).

Under an identical applied voltage of 30 V, both the resultant currents and nanosheet concentrations varied largely across different solvents. Figure 3e summarizes the relationship among solvent permittivity, generated current, and nanosheet concentration. Clearly, high solvent permittivity correlates with increased currents that promote delamination of the TpPa film. Nanosheet concentration also increases with solvent permittivity, with a threshold permittivity of ∼10 F m^{-1} for efficient nanosheet production. The addition of PTSA was demonstrated to improve the delamination efficiency for the moderate-permittivity solvents (Figure S31). Control experiments without PTSA show minor currents and limited delamination for these solvents (Table S3), despite the formation of nanosheets (Figure S32). Notably, the moderate-permittivity solvents can achieve high delamination efficiencies comparable to DMF and DMSO when PTSA was added (Figures S33, S34). This enhancement is attributed to the dissociation of PTSA in these solvents, generating free ions that improve conductivity and enhance current density.

To elucidate the relationship between solvent parameters and delamination efficiency, we performed principal component analysis (PCA), which reduces correlated variables into independent components ranked by their contributions to the total variance. The PCA score plot categorizes solvents into three clusters: DMF and DMSO, alcohols, and low-permittivity solvents (dioxane, *n*-hexane, and ethyl acetate) (Figure 3f and Table S4). The loading plot highlights strong positive correlations between nanosheet concentration and both permittivity and polarity, suggesting their domination in promoting delamination. The close alignment of permittivity and polarity vectors indicates their strong correlation, whereas the solvent size shows minimal impact, as reflected by its distant placement from the concentration vector. Moreover, the generated current shows a moderate correlation with delamination efficiency, suggesting that beyond a certain threshold, further current increases barely enhance delamination. Collectively, the selection of solvents for efficient electrochemical delamination is primarily governed by their permittivity, polarity, and wettability. Solvents with moderate to high permittivity and good wetting ability toward the film, especially in the presence of PTSA, facilitate delamination by delivering higher current densities under identical applied voltage. These insights provide valuable guidelines for optimizing electrolytes to enhance the efficiency of electrochemical delamination.

Current-Dependent Electrochemical Delamination Dynamics. As illustrated in Figure 4a, the electrochemical delamination of TpPa films in an ethanol–PTSA electrolyte follows a multistep synergistic mechanism, integrating structural preintercalation, electrostatic repulsion, and gas-driven mechanical expansion. During film preparation, PTSA functions as both a catalyst and an intercalating agent, embedding within the film interlayers. This preintercalation expands the interlayer spacing and weakens van der Waals (vdW) forces between layers, thereby lowering the energy barrier for subsequent delamination. PXRD analysis shows that the (001) diffraction of the PTSA-catalyzed TpPa film exhibits an obvious low-angle shift compared to that prepared using acetic acid (Figures S35–S37). This indicates an enlarged interlayer spacing that is decisive for effectual delamination. By contrast, the acetic acid-catalyzed TpPa film, which possesses tighter stacking, shows minimal delamination efficiency under identical electrochemical conditions (Figure S38).

Upon application of an electric field, the delamination proceeds through two complementary mechanisms involving electrostatic repulsion and gas-driven mechanical expansion. In ethanol, PTSA dissociates into H^+ and *p*-toluenesulfonate (TOS^-) ions. Under an applied bias, H^+ selectively protonates electron-rich enamine linkages, generating positive charges along the TpPa layers. This protonation-induced charge accumulation generates interlayer electrostatic repulsion, weakening vdW interactions and facilitating film disintegration. Simultaneously, TOS^- anions could intercalate into the film interlayers, imposing steric strain that further destabilizes the film.[44] The synergy of protonation-induced repulsion and steric destabilization primes the film for delamination. Concurrently, vigorous gas evolution at both electrodes exerts additional mechanical forces that promote exfoliation (Video S1).[45] Gas chromatography analysis confirms the generation of H_2 at the cathode and a mixture of CO, O_2, and CH_4 at the anode (Figures 4b, S39), with gas generation rates reaching approximately 1.3 mL min^{-1} (cathode) and 0.1 mL min^{-1} (anode) at 200 mA. This rapid gas generation introduces significant interspace stress within the TpPa framework, mechanically assisting the delamination process.[46] Postdelamination analysis of the residual TpPa film reveals a distinctively expanded and completely fragmented morphology (Figure S40), showing the combined effects of charge repulsion and gas-driven expansion.

The applied current density plays a pivotal role in governing the delamination efficiency and structural order. Without an applied bias, no delamination of films occurs (Figure S41), confirming the indispensable role of applying currents. As the applied current increases from 50 to 500 mA, enhanced protonation and accelerated gas evolution promote the delamination efficiency (Figures S42 and S43). However, this comes at the expense of structural order, as evidenced by progressive declines in the (100) diffraction intensity and BET surface area of both TpPa nanosheets and residual films (Figures 4c and S44–S46). The weakened and broadened diffraction peak from the (001) plane after the electrochemical process confirms the occurrence of delamination (Figure S47). To elucidate the relationship between the protonation degree and current density, we conducted ^{13}C solid-state NMR and XPS analyses. A signal at 61.7 ppm in the NMR spectrum, attributed to protonated $C-N^+$ sites, intensifies with an increasing current (Figure 4d). XPS C 1s spectra in Figure 4e also show the emergence and progressive growth of a distinct $C-N^+$ component with its relative proportion increasing at higher currents. Complementary FTIR results corroborate this trend, showing increasingly pronounced stretching vibrations at 1607 cm^{-1} (Figure S48), characteristic of protonated enamine linkages.

Nanosheet thickness exhibits a clear current-dependent trend. SEM and AFM analyses reveal that nanosheets exfoliated at lower currents such as 200 and 300 mA are thinner, typically below 4 nm (Figures S49, S50). In comparison, high currents produce nanosheets exceeding 30 nm in thickness, due to excessive gas evolution and overprotonation. In addition, TEM images visualize the

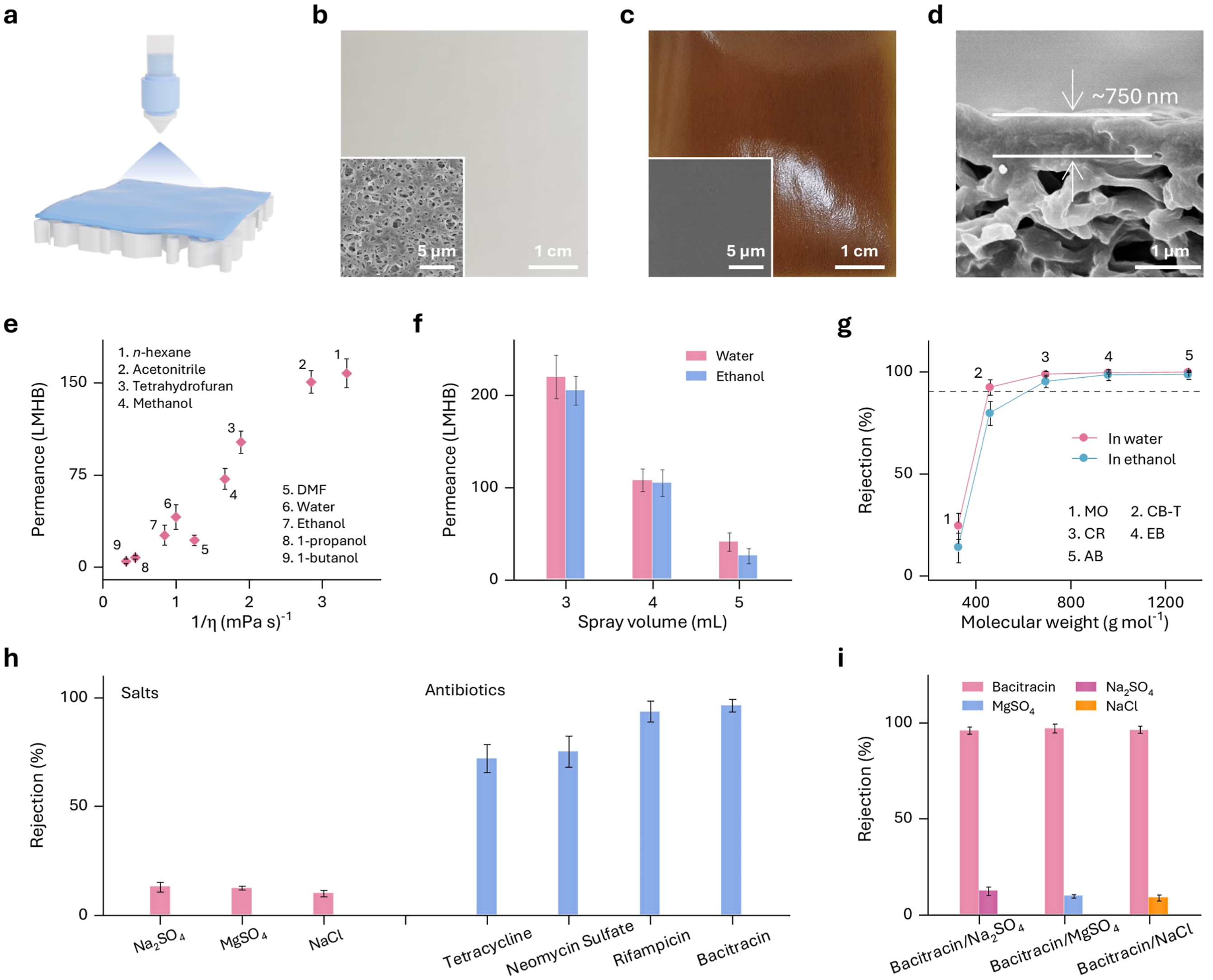

Figure 5. TpPa nanosheet membranes for antibiotic desalination. (a) Schematic illustration of spray-coating to produce TpPa-200 membranes. Photographs of (b) the nylon support and (c) the 5 mL TpPa-200 membrane. (d) Cross-sectional SEM image of the 5 mL TpPa-200 membrane. (e) Solvent permeance as a function of reciprocal viscosity. (f) Water and ethanol permeance. (g) Molecular rejections in water and ethanol. (h) Rejections of salts and antibiotics in water. (i) Separation performance of mixed antibiotic-salt solutions. Insets in (b,c) show the surface SEM images of the nylon support and the 5 mL TpPa-200 membrane, respectively.

structural evolution of the nanosheets exfoliated under different current conditions (Figure 4f). Specifically, the nanosheets produced at 200 mA show well-defined lattice fringes indicative of retained structural order, which is consistent with the PXRD findings. Increasing the current from 300 to 500 mA results in nanosheets with progressively attenuated lattice fringes, suggesting cumulative structural degradation possibly driven by overprotonation and intense mechanical stress. Thus, a current value of 200 mA is recognized as optimal for the efficient production of high-quality TpPa nanosheets.

TpPa Nanosheet Membranes for Antibiotic Desalination. Our strategy enabled scalable production of well-dispersed, crystalline TpPa-200 nanosheets, offering excellent processability for membrane fabrication.[47] Here, we employed an industrially scalable spray-coating approach to assemble TpPa-200 nanosheets into large-area membranes for molecular separation (Figure 5a). Low-cost, commercially available nylon membranes with macroporous structures were chosen as the substrate, providing mechanical stability and facilitating uniform nanosheet deposition (Figure 5b). As shown in Figure 5c, spray-coating produces defect-free continuous membranes with a well-defined selective layer. Cross-sectional SEM imaging further reveals tight adhesion of a 750 nm-thick TpPa-200 layer on the nylon substrate (Figure 5d). Notably, the nanosheet layer thickness is tunable in the range of 350–750 nm by adjusting the spray volume (Figures S51 and S52).

Solvent permeation tests of the TpPa-200 membrane with a 5 mL spray volume reveal a near-linear correlation between solvent permeance and reciprocal viscosity, aligning with the Hagen–Poiseuille equation (Figure 5e). This suggests that solvent transport is primarily governed by intrinsic membrane porosity and viscosity-dependent flow dynamics.[48] To evaluate the separation performance, TpPa-200 membranes with varying spray volumes were tested (Figure 5f). Increasing the spray volume from 3 to 5 mL results in a progressive decrease in water and ethanol permeance due to enhanced mass transport resistance from the thickened selective layer. Simultaneously, molecular rejection increases with increasing spray volume (Figure S53). Specifically, the membrane with a

3 mL spray volume exhibits a high water permeance of 220 L m^2 h^{-1} bar^{-1} (LMHB) and an ethanol permeance of 205 LMHB, which declines to 41 and 25 LMHB, respectively, when the volume increases to 5 mL. Moreover, Congo red (CR, M_w = 696 g mol^{-1}) rejection increases from 97.9% to 98.8% in water and from 82.2% to 95.2% in ethanol. Further molecular separation analysis of the 5 mL TpPa-200 membrane was performed using solutes with molecular weights ranging from ∼300 to ∼1300 g mol^{-1} (Figure S54). Rejection profiles show that the membrane affords molecular weight cutoffs (MWCOs) of 450 g mol^{-1} in water and 610 g mol^{-1} in ethanol (Figures 5g, S55, and S56). The observed MWCO discrepancy likely arises from weakened electrostatic interactions in ethanol,[49] suggesting the efficacy of size exclusion by intrinsic TpPa-200 pores. This molecular separation capability further enables the efficient rejection of value-added biomolecules with adequate antifouling performance (Figures S57−S60), offering potential for biological wastewater treatment and biomolecule purification.

Antibiotics are primarily produced through bacterial fermentation, which necessitates the addition of inorganic salts to sustain biological activity.[50,51] Consequently, the removal of these salts is a critical step in obtaining high-purity antibiotics, a process referred to as antibiotic desalination.[52] To assess the antibiotic desalination performance of the 5 mL TpPa-200 membrane, we tested representative inorganic salts (Na_2SO_4, $MgSO_4$, NaCl) alongside antibiotics (tetracycline, rifampicin, neomycin sulfate, bacitracin) (Figure S61). As shown in Figure 5h, the membrane shows low salt rejections of below 13% due to the substantial size difference between the TpPa-200 pore and hydrated ions while giving high rejections for rifampicin and bacitracin (Figure S62). Leveraging this selective exclusion capability, the membrane achieves a high separation performance in binary-component systems containing bacitracin and salts, outperforming previously reported membranes (Figure 5i, Table S5). The antibiotic desalination performance remains relatively stable after 5-cycle reuse and 14 h of continuous operation (Figures S63, S64). These demonstrate the practical applicability of our membrane for antibiotic desalination in pharmaceutical purification workflows, where selective antibiotic retention with efficient salt removal is highly desirable.

CONCLUSIONS

In summary, we have demonstrated a scalable and efficient electrochemical strategy for the nearly nondestructive delamination of polycrystalline 2D COF films into crystalline nanosheets with long-range structural order. This method achieves a prominent delamination throughput of up to 14.1 mg L^{-1} min^{-1} and produces nanosheets that form exceptionally stable dispersions in both organic and aqueous media. Through principal component analysis and comprehensive structural characterizations, we identify solvent permittivity, polarity, and film wettability as critical determinants of delamination efficiency and elucidate a synergistic mechanism involving intercalation, charge repulsion, and physical exfoliation. We further illustrate the practical use of these porous crystalline nanosheets by fabricating high-performance membranes for efficient antibiotic desalination. Overall, this work provides a robust pathway toward the scaling-up of crystalline COF nanosheets and opens new possibilities for the deployment of COFs across diverse fields.

ASSOCIATED CONTENT

Supporting Information

The Supporting Information is available free of charge at https://pubs.acs.org/doi/10.1021/jacs.5c06026.

Experimental details; molecular structures; digital photos; SEM images; HRTEM images; FFT patterns; AFM images; FTIR spectra; PXRD patterns; N_2 sorption isotherms; zeta potential; dynamic light scattering curves; contact angles; UV−vis spectra; and membrane tests (PDF)

Electrochemical delamination of the TpPa film in ethanol under 200 mA (MP4)

AUTHOR INFORMATION

Corresponding Authors

Xiansong Shi − *State Key Laboratory of Materials-Oriented Chemical Engineering, College of Chemical Engineering, Nanjing Tech University, Nanjing 211816 Jiangsu, China;* orcid.org/0000-0002-4258-7941; Email: xsshi@njtech.edu.cn

Yong Wang − *State Key Laboratory of Materials-Oriented Chemical Engineering, College of Chemical Engineering, Nanjing Tech University, Nanjing 211816 Jiangsu, China; School of Energy and Environment, Southeast University, Nanjing 210096 Jiangsu, China;* orcid.org/0000-0002-8653-514X; Email: yongwang@seu.edu.cn

Authors

Tong Ju − *State Key Laboratory of Materials-Oriented Chemical Engineering, College of Chemical Engineering, Nanjing Tech University, Nanjing 211816 Jiangsu, China;* orcid.org/0009-0001-1471-6347

Zhenshu Si − *State Key Laboratory of Materials-Oriented Chemical Engineering, College of Chemical Engineering, Nanjing Tech University, Nanjing 211816 Jiangsu, China;* orcid.org/0009-0007-3373-2717

Tianci Feng − *State Key Laboratory of Materials-Oriented Chemical Engineering, College of Chemical Engineering, Nanjing Tech University, Nanjing 211816 Jiangsu, China;* orcid.org/0000-0001-7176-0005

Jianghai Long − *State Key Laboratory of Materials-Oriented Chemical Engineering, College of Chemical Engineering, Nanjing Tech University, Nanjing 211816 Jiangsu, China;* orcid.org/0009-0009-6392-3842

Congcong Yin − *School of Energy and Environment, Southeast University, Nanjing 210096 Jiangsu, China;* orcid.org/0000-0002-1533-8018

Zhe Zhang − *School of Environmental Science and Engineering, Nanjing Tech University, Nanjing 211816 Jiangsu, China;* orcid.org/0000-0003-0523-0262

Complete contact information is available at: https://pubs.acs.org/10.1021/jacs.5c06026

Notes

The authors declare the following competing financial interest(s): Nanjing Tech University has filed the patent application related to the findings described in this work.

ACKNOWLEDGMENTS

This work was supported by the National Natural Science Foundation of China (U24A2083) and the National Key

Research and Development Program of China (2022YFB3805201).

■ REFERENCES

(1) Novoselov, K. S.; Geim, A. K.; Morozov, S. V.; Jiang, D.; Zhang, Y.; Dubonos, S. V.; Grigorieva, I. V.; Firsov, A. A. Electric field effect in atomically thin carbon films. *Science* **2004**, *306*, 666−669.

(2) Novoselov, K. S.; Mishchenko, A.; Carvalho, A.; Castro Neto, A. H. 2D materials and van der Waals heterostructures. *Science* **2016**, *353*, aac9439.

(3) Tan, C. L.; Cao, X. H.; Wu, X. J.; He, Q. Y.; Yang, J.; Zhang, X.; Chen, J. Z.; Zhao, W.; Han, S. K.; Nam, G. H.; Sindoro, M.; Zhang, H. Recent advances in ultrathin two-dimensional nanomaterials. *Chem. Rev.* **2017**, *117*, 6225−6331.

(4) Huang, X.; Qi, X.; Boey, F.; Zhang, H. Graphene-based composites. *Chem. Soc. Rev.* **2012**, *41*, 666−686.

(5) Chhowalla, M.; Shin, H. S.; Eda, G.; Li, L. J.; Loh, K. P.; Zhang, H. The chemistry of two-dimensional layered transition metal dichalcogenide nanosheets. *Nat. Chem.* **2013**, *5*, 263−275.

(6) Chhowalla, M.; Liu, Z. F.; Zhang, H. Two-dimensional transition metal dichalcogenide (TMD) nanosheets. *Chem. Soc. Rev.* **2015**, *44*, 2584−2586.

(7) Yang, Y. C.; Song, Z. G.; Lu, G. Y.; Zhang, Q. H.; Zhang, B. Y.; Ni, B.; Wang, C.; Li, X. Y.; Gu, L.; Xie, X. M.; Gao, H. J.; Lou, J. Intrinsic toughening and stable crack propagation in hexagonal boron nitride. *Nature* **2021**, *594*, 57−61.

(8) Tran, T. T.; Bray, K.; Ford, M. J.; Toth, M.; Aharonovich, I. Quantum emission from hexagonal boron nitride monolayers. *Nat. Nanotechnol.* **2016**, *11*, 37−41.

(9) Wyatt, B. C.; Rosenkranz, A.; Anasori, B. 2D MXenes: tunable mechanical and tribological properties. *Adv. Mater.* **2021**, *33*, 2007973.

(10) Naguib, M.; Mochalin, V. N.; Barsoum, M. W.; Gogotsi, Y. 25th anniversary article: MXenes: a new family of two-dimensional materials. *Adv. Mater.* **2014**, *26*, 992−1005.

(11) Côté, A. P.; Benin, A. I.; Ockwig, N. W.; O'Keeffe, M.; Matzger, A. J.; Yaghi, O. M. Porous, crystalline, covalent organic frameworks. *Science* **2005**, *310*, 1166−1170.

(12) Ding, S. Y.; Wang, W. Covalent organic frameworks (COFs): from design to applications. *Chem. Soc. Rev.* **2013**, *42*, 548−568.

(13) Yin, C. C.; Liu, M.; Zhang, Z.; Wei, M. J.; Shi, X. S.; Zhang, Y. T.; Wang, J. T.; Wang, Y. Perpendicular alignment of covalent organic framework (COF) pore channels by solvent vapor annealing. *J. Am. Chem. Soc.* **2023**, *145*, 11431−11439.

(14) Shinde, D. B.; Sheng, G.; Li, X.; Ostwal, M.; Emwas, A. H.; Huang, K. W.; Lai, Z. P. Crystalline 2D covalent organic framework membranes for high-flux organic solvent nanofiltration. *J. Am. Chem. Soc.* **2018**, *140*, 14342−14349.

(15) Jin, Y. H.; Hu, Y. M.; Zhang, W. Tessellated multiporous two-dimensional covalent organic frameworks. *Nat. Rev. Chem.* **2017**, *1*, 0056.

(16) Mahato, A. K.; Paul, S.; Banerjee, R. Synthesis innovations for crystallizing covalent organic framework thin films on biological and non-biological substrates. *Chem. Soc. Rev.* **2025**, *54*, 3578−3598.

(17) Ren, Y. M.; Xu, Y. X. Recent advances in two-dimensional polymers: synthesis, assembly and energy-related applications. *Chem. Soc. Rev.* **2024**, *53*, 1823−1869.

(18) Shi, X. S.; Li, H.; Chen, T.; Ren, J. Y.; Zhao, W.; Patra, B. C.; Kang, C. J.; Zhang, Z. Q.; Zhao, D. Precise separation of complex ultrafine molecules through solvating two-dimensional covalent organic framework membranes. *Angew. Chem., Int. Ed.* **2025**, *64*, No. e20242166.

(19) Yin, C. C.; Li, Z.; Zhao, D. C.; Yang, J. Y.; Zhang, Y.; Du, Y.; Wang, Y. Azo-branched covalent organic framework thin films as active separators for superior sodium-sulfur batteries. *ACS Nano* **2022**, *16*, 14178−14187.

(20) Haase, F.; Lotsch, B. V. Solving the COF trilemma: towards crystalline, stable and functional covalent organic frameworks. *Chem. Soc. Rev.* **2020**, *49*, 8469−8500.

(21) Wang, S.; Reddy, V. A.; Ang, M. C. Y.; Cui, J. Q.; Khong, D. T.; Han, Y. Y.; Loh, S. I.; Cheerlavancha, R.; Singh, G. P.; Rajani, S.; Strano, M. S. Single-crystal 2D covalent organic frameworks for plant biotechnology. *J. Am. Chem. Soc.* **2023**, *145*, 12155−12163.

(22) Zhou, Z. B.; Han, X. H.; Qi, Q. Y.; Gan, S. X.; Ma, D. L.; Zhao, X. A facile, efficient, and general synthetic method to amide-linked covalent organic frameworks. *J. Am. Chem. Soc.* **2022**, *144*, 1138−1143.

(23) Duan, H. Y.; Li, K.; Xie, M.; Chen, J. M.; Zhou, H. G.; Wu, X. F.; Ning, G. H.; Cooper, A. I.; Li, D. Scalable synthesis of ultrathin polyimide covalent organic framework nanosheets for high-performance lithium-sulfur batteries. *J. Am. Chem. Soc.* **2021**, *143*, 19446−19453.

(24) Liu, X. L.; Jin, Y. C.; Wang, H. L.; Yang, X. Y.; Zhang, P. P.; Wang, K.; Jiang, J. Z. In situ growth of covalent organic framework nanosheets on graphene as the cathode for long-life high-capacity lithium-ion batteries. *Adv. Mater.* **2022**, *34*, 2203605.

(25) Liu, W. B.; Li, X. K.; Wang, C. M.; Pan, H. H.; Liu, W. P.; Wang, K.; Zeng, Q. D.; Wang, R. M.; Jiang, J. Z. A scalable general synthetic approach toward ultrathin imine-linked two-dimensional covalent organic framework nanosheets for photocatalytic CO_2 reduction. *J. Am. Chem. Soc.* **2019**, *141*, 17431−17440.

(26) Huang, T.; Jiang, H.; Douglin, J. C.; Chen, Y.; Yin, S.; Zhang, J.; Deng, X.; Wu, H.; Yin, Y.; Dekel, D. R.; Guiver, M. D.; Jiang, Z. Single solution-phase synthesis of charged covalent organic framework nanosheets with high volume yield. *Angew. Chem., Int. Ed.* **2023**, *62*, No. e202209306.

(27) Sun, T.; Li, S.; Zhang, L.; Xu, Y. Aqueous processable two-dimensional triazine polymers with superior photocatalytic properties. *Angew. Chem., Int. Ed.* **2023**, *62*, No. e202301865.

(28) Chandra, S.; Kandambeth, S.; Biswal, B. P.; Lukose, B.; Kunjir, S. M.; Chaudhary, M.; Babarao, R.; Heine, T.; Banerjee, R. Chemically stable multilayered covalent organic nanosheets from covalent organic frameworks via mechanical delamination. *J. Am. Chem. Soc.* **2013**, *135*, 17853−17861.

(29) Khayum, M. A.; Kandambeth, S.; Mitra, S.; Nair, S. B.; Das, A.; Nagane, S. S.; Mukherjee, R.; Banerjee, R. Chemically delaminated free-standing ultrathin covalent organic nanosheets. *Angew. Chem., Int. Ed.* **2016**, *55*, 15604−15608.

(30) Burke, D. W.; Sun, C.; Castano, I.; Flanders, N. C.; Evans, A. M.; Vitaku, E.; McLeod, D. C.; Lambeth, R. H.; Chen, L. X.; Gianneschi, N. C.; Dichtel, W. R. Acid exfoliation of imine-linked covalent organic frameworks enables solution processing into crystalline thin films. *Angew. Chem., Int. Ed.* **2020**, *59*, 5165−5171.

(31) Peng, Y.; Huang, Y.; Zhu, Y.; Chen, B.; Wang, L.; Lai, Z.; Zhang, Z.; Zhao, M.; Tan, C.; Yang, N.; Shao, F.; Han, Y.; Zhang, H. Ultrathin two-dimensional covalent organic framework nanosheets: preparation and application in highly sensitive and selective DNA detection. *J. Am. Chem. Soc.* **2017**, *139*, 8698−8704.

(32) Yang, S.; Zhang, P. P.; Nia, A. S.; Feng, X. L. Emerging 2D materials produced via electrochemistry. *Adv. Mater.* **2020**, *32*, 1907857.

(33) Parvez, K.; Wu, Z. S.; Li, R. J.; Liu, X. J.; Graf, R.; Feng, X. L.; Müllen, K. Exfoliation of graphite into graphene in aqueous solutions of inorganic salts. *J. Am. Chem. Soc.* **2014**, *136*, 6083−6091.

(34) Acerce, M.; Voiry, D.; Chhowalla, M. Metallic 1T phase MoS_2 nanosheets as supercapacitor electrode materials. *Nat. Nanotechnol.* **2015**, *10*, 313−318.

(35) Jeon, I.; Yoon, B.; He, M.; Swager, T. M. Hyperstage graphite: electrochemical synthesis and spontaneous reactive exfoliation. *Adv. Mater.* **2018**, *30*, 1704538.

(36) Lin, Z. Y.; Liu, Y.; Halim, U.; Ding, M. N.; Liu, Y. Y.; Wang, Y. L.; Jia, C. C.; Chen, P.; Duan, X. D.; Wang, C.; Song, F.; Li, M. F.; Wan, C. Z.; Huang, Y.; Duan, X. F. Solution-processable 2D semiconductors for high-performance large-area electronics. *Nature* **2018**, *562*, 254−258.

(37) Li, J.; Song, P.; Zhao, J. P.; Vaklinova, K.; Zhao, X. X.; Li, Z. J.; Qiu, Z. Z.; Wang, Z. H.; Lin, L.; Zhao, M.; Herng, T. S.; Zuo, Y. X.; Jonhson, W.; Yu, W.; Hai, X.; Lyu, P.; Xu, H. M.; Yang, H. M.; Chen,

C.; Pennycook, S. J.; Ding, J.; Teng, J. H.; Castro Neto, A. H.; Novoselov, K. S.; Lu, J. Printable two-dimensional superconducting monolayers. *Nat. Mater.* **2021**, *20*, 181−187.

(38) Yang, R. J.; Mei, L.; Zhang, Q. Y.; Fan, Y. Y.; Shin, H. S.; Voiry, D.; Zeng, Z. Y. High-yield production of mono- or few-layer transition metal dichalcogenide nanosheets by an electrochemical lithium ion intercalation-based exfoliation method. *Nat. Protoc.* **2022**, *17*, 358−377.

(39) Wang, L. L.; Xu, C. W.; Zhang, W. Q.; Zhang, Q. L.; Zhao, M. L.; Zeng, C.; Jiang, Q. L.; Gu, C.; Ma, Y. G. Electrocleavage synthesis of solution-processed, imine-linked, and crystalline covalent organic framework thin films. *J. Am. Chem. Soc.* **2022**, *144*, 8961−8968.

(40) Kandambeth, S.; Biswal, B. P.; Chaudhari, H. D.; Rout, K. C.; Kunjattu H, S.; Mitra, S.; Karak, S.; Das, A.; Mukherjee, R.; Kharul, U. K.; Banerjee, R. Selective molecular sieving in self-standing porous covalent-organic-framework membranes. *Adv. Mater.* **2017**, *29*, 1603945.

(41) Kandambeth, S.; Mallick, A.; Lukose, B.; Mane, M. V.; Heine, T.; Banerjee, R. Construction of crystalline 2D covalent organic frameworks with remarkable chemical (acid/base) stability via a combined reversible and irreversible route. *J. Am. Chem. Soc.* **2012**, *134*, 19524−19527.

(42) Song, Y.; Zhang, J. J.; Dou, Y.; Zhu, Z.; Su, J.; Huang, L.; Guo, W.; Cao, X.; Cheng, L.; Zhu, Z.; Zhang, Z.; Zhong, X.; Yang, D.; Wang, Z.; Tang, B. Z.; Yakobson, B. I.; Ye, R. Atomically thin, ionic-covalent organic nanosheets for stable, high-performance carbon dioxide electroreduction. *Adv. Mater.* **2022**, *34*, 2110496.

(43) Haldar, S.; Roy, K.; Kushwaha, R.; Ogale, S.; Vaidhyanathan, R. Chemical exfoliation as a controlled route to enhance the anodic performance of COF in LIB. *Adv. Energy Mater.* **2019**, *9*, 1902428.

(44) Wang, S. Q.; Xue, J. Y.; Xu, D.; He, J.; Dai, Y. P.; Xia, T. Y.; Huang, Y.; He, Q. Y.; Duan, X. F.; Lin, Z. Y. Electrochemical molecular intercalation and exfoliation of solution-processable two-dimensional crystals. *Nat. Protoc.* **2023**, *18*, 2814−2837.

(45) Liu, N.; Kim, P.; Kim, J. H.; Ye, J. H.; Kim, S.; Lee, C. J. Large-area atomically thin MoS_2 nanosheets prepared using electrochemical exfoliation. *ACS Nano* **2014**, *8*, 6902−6910.

(46) Zhou, Y.; Wu, Y.; Wu, H.; Xue, J.; Ding, L.; Wang, R.; Wang, H. Fast hydrogen purification through graphitic carbon nitride nanosheet membranes. *Nat. Commun.* **2022**, *13*, 5852.

(47) Ju, T.; Liu, M.; Shi, X. S.; Xiao, A. K.; Zhang, Z.; Wang, J. T.; Zhang, Y. T.; Wang, Y. Chemically asymmetric polymers manipulate the crystallization of two-dimensional covalent organic frameworks to synthesize processable nanosheets. *ACS Nano* **2023**, *17*, 23784−23793.

(48) Silva, P.; Han, S.; Livingston, A. G. Solvent transport in organic solvent nanofiltration membranes. *J. Membr. Sci.* **2005**, *262*, 49−59.

(49) Wang, X. Y.; Yang, J. Y.; Shi, X. S.; Zhang, Z.; Yin, C. C.; Wang, Y. Electrosynthesis of ionic covalent organic frameworks for charge-selective separation of molecules. *Small* **2022**, *18*, 2107108.

(50) Ren, L. F.; Zhang, S. Q.; Ma, Z. B.; Qiu, Y. B.; Ying, D. W.; Jia, J. P.; Shao, J. H.; He, Y. L. Antibiotics separation from saline wastewater by nanofiltration membrane based on tannic acid-ferric ions coordination complexes. *Desalination* **2022**, *541*, 116034.

(51) Wang, C. C.; Sun, H.; Wang, N. X.; An, Q. F. Robust ZIF-8 and its derivative composite membrane for antibiotic desalination with high performance. *Sep. Purif. Technol.* **2023**, *307*, 122857.

(52) Bai, Y. X.; Liu, B. B.; Li, J. C.; Li, M. H.; Yao, Z.; Dong, L. L.; Rao, D. W.; Zhang, P.; Cao, X. Z.; Villalobos, L. F.; Zhang, C. F.; An, Q. F.; Elimelech, M. Microstructure optimization of bioderived polyester nanofilms for antibiotic desalination via nanofiltration. *Sci. Adv.* **2023**, *9*, No. eadg6134.